Research Square

Preprints are preliminary reports that have not undergone peer review.
They should not be considered conclusive, used to inform clinical practice,
or referenced by the media as validated information.

Superbunched random fiber laser

Yanping Xu

yanpingxu@sdu.edu.cn

Shandong University

Qiang Ji

Shandong University

Yuxi Pang

Shandong University

Weiming Zhang

Shandong University

Xian Zhao

State Key Laboratory of Crystal Materials, Institute of Crystal Materials, Shandong University

Zengguang Qin

Shandong University

Zhaojun Liu

Shandong University

Article

Keywords:

Posted Date: July 27th, 2026

DOI: https://doi.org/10.21203/rs.3.rs-10170245/v1

License: This work is licensed under a Creative Commons Attribution 4.0 International License.
Read Full License

Additional Declarations: There is **NO** Competing Interest.

Superbunched random fiber laser

Abstract

Photon superbunching, with second-order coherence far beyond the Gaussian thermal limit, is a valuable resource for quantum optics and correlation-based imaging. However, existing sources often rely on fragile platforms, inefficient nonlinear conversion, or mechanically complex architectures. Here, we demonstrate the first highly stable, fully fiber-integrated superbunched random fiber laser that provides a broadly tunable source of giant photon bunching. We establish a cooperative linear–nonlinear mechanism in which Rayleigh-scattering-mediated diffusion provides distributed random feedback, while cascaded stimulated Brillouin scattering and quasi-phase-matched four-wave mixing amplify and redistribute stochastic intensity fluctuations across a spectral comb. This enables continuous tuning of $g^{(2)}(0)$ from approximately 1 to 28 via tailored modulation of linear diffusion strength and nonlinear coupling magnitude. Moreover, by combining photon-correlation measurements with Parisi-overlap analysis, we reveal an inverse correlation between disorder-induced photonic phase evolution and microscopic photon bunching, bridging macroscopic disordered-cavity dynamics and high-order photon statistics. Furthermore, we demonstrate that strongly superbunched light enables temporal ghost imaging with comparable reconstruction fidelity while requiring more than an order-of-magnitude fewer realizations than weakly bunched light. Together, these results establish a fiber-integrated route to engineering giant photon superbunching and high-order light statistics for correlation-based photonic technologies.

Random fiber lasers[1,2,3] (RFLs) provide a versatile platform for investigating light-matter interactions in disordered photonic media. The random distributed feedback resulting from Rayleigh scattering, combined with gain and nonlinear interactions, has enabled the observation of Anderson localization[4], optical rogue waves[5,6], replica symmetry breaking[7,8] and non-equilibrium photonic phase transitions[9] in one-dimensional fiber systems. These pioneering studies have elucidated the fundamental mechanisms by which disorder, distributed feedback and nonlinearity collectively govern the macroscopic optical behavior of RFLs[10,11]. However, most reported work has characterized RFLs using conventional spectral, temporal, or phase-transition diagnostics, without a correlation-resolved view of

their photon statistics[5-9,12-16]. The photon statistics and higher-order coherence properties of RFLs, particularly in operating regimes with strong disorder and cascaded nonlinear processes, remain largely unexplored[17,18]. This critical knowledge gap restricts the utility of RFLs as model systems for quantum optics studies in complex photonic media and constrains their practical impact on correlation-based optical sensing and imaging technologies[18-20].

The second-order coherence function $g^{(2)}(\tau)$ is a foundational quantity for characterizing photon statistics and quantum optical behavior[21-24]. Its zero-delay value $g^{(2)}(0)$ distinguishes coherent light with $g^{(2)}(0)=1$, thermal or chaotic light with Gaussian field statistics and $1<g^{(2)}(0)\leq 2$, and non-classical light fields such as antibunched single-photon streams with $g^{(2)}(0)<1$. Superbunching, defined as a $g^{(2)}(0)$ value far exceeding the Gaussian-statistics thermal (chaotic) limit of 2, corresponds to extreme photon clustering and enhanced correlation contrast, which can benefit correlation-based sensing and ghost imaging[25,26]. Existing approaches to generating superbunched light have primarily relied on nonlinear optical interactions in atomic and semiconductor systems[27-33], or linear optical schemes based on multi-photon interference and mechanically modulated diffusers[34-39]. Yet these platforms often face low conversion efficiency, narrow bandwidth, stringent stability requirements, or limited scalability. RFLs are intrinsically fluctuation-rich optical systems: distributed Rayleigh scattering furnishes a dense ensemble of random feedback pathways, while third-order nonlinear optical processes, including stimulated Brillouin scattering (SBS) and four-wave mixing (FWM), endow the cavity with robust nonlinear gain and efficient intermodal coupling. Despite this potential, RFLs have generally been treated as conventional or quasi-thermal sources, and a clear connection between disorder-driven photonic phase evolution and microscopic photon statistics has not been established.

In this work, we demonstrate a fully fiber-integrated superbunched random fiber laser (SRFL) in which intrinsic Rayleigh scattering cooperates with cascaded nonlinear interactions, specifically cascaded stimulated Brillouin scattering (CSBS) and quasi-phase-matched FWM, to engineer extreme photon statistics in a deterministic manner. The SRFL emits a comb, where individual spectral components exhibit tunable photon bunching with $g^{(2)}(0)$ values adjustable from ~1 to ~28 via tailored modulation of linear diffusion strength and nonlinear coupling magnitude. Photon-correlation measurements combined with Parisi-overlap analysis reveal an inverse correlation between enhanced superbunching and macroscopic replica overlap, linking disorder-driven phase evolution to microscopic photon statistics. Building on this controllable photon-superbunching behavior, we demonstrate

temporal ghost imaging (TGI) [40-42], where strongly superbunched illumination achieves comparable reconstruction quality with more than an order-of-magnitude reduction in the required number of realizations compared with weakly bunched illumination.

Results

Operating principle

The fundamental mechanism governing superbunching in the SRFL is illustrated in **Figs. 1a-c**. This extreme photon clustering phenomenon arises from the synergistic interplay between disorder-induced linear diffusion in the passive Rayleigh scattering fiber (RSF) and cascaded nonlinear optical interactions in the Brillouin gain fiber (BGF). As depicted in **Fig. 1a**, a continuous-wave pump is launched into the BGF where electrostriction-induced acoustic phonon excitation triggers SBS and generates the back-propagating Stokes emission. This Stokes light subsequently propagates into the RSF, where it undergoes multiple stochastic Rayleigh scattering events. A fraction of the backscattered Stokes light is returned into the BGF, counter-propagating with the incident pump, to form a Rayleigh-scattering-mediated one-dimensional diffusion process (**Fig. 1c**), which provides distributed feedback and seeds subsequent Brillouin amplification.

Tailoring the length of the RSF enables control of the strength of this random feedback and the baseline level of intracavity intensity fluctuations. Within the RSF, interference among many indistinguishable scattering pathways creates a fluctuation-rich optical background that seeds photon bunching. Once these Rayleigh-seeded fluctuations are fed back into the BGF, CSBS transfers optical energy and intensity fluctuations from the pump to successive Stokes orders, while quasi-phase-matched FWM couples the pump, Stokes and anti-Stokes fields and further redistributes the fluctuations across the comb **(Fig. 1b)**. The combined action of linear diffusion and cascaded nonlinear conversion gives rise to order-dependent superbunching. Each spectral component contains many narrow random-cavity modes participating in CSBS and FWM, increasing the degrees of freedom, promoting inter-mode competition and redistributing intensity fluctuations across the comb. A theoretical description of this cascaded fluctuation-transfer mechanism based on a Heisenberg–Langevin framework is provided in **Methods.**

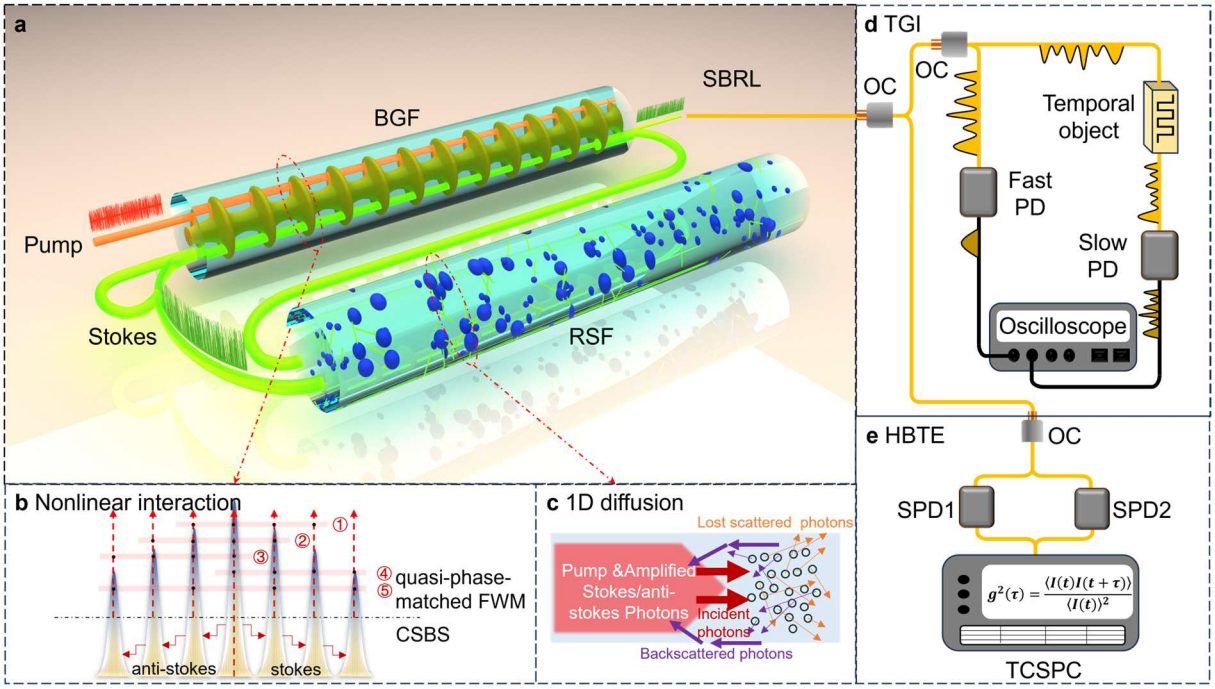


Fig. 1 | Integrated architecture and operating principles of the SRFL, temporal ghost imaging system, and second-order coherence measurement system. a, Schematic of the SRFL mainly composed of a BGF and an RSF. **b**, Nonlinear interactions inside the BGF, including the CSBS and quasi-phase-matched FWM processes. **c**, One-dimensional random diffusion inside the RSF provided by the Rayleigh scattering process. **d**, Temporal ghost imaging setup. **e**, HBT experiment setup for measuring second-order coherence. SRFL, superbunched random fiber laser; TGI, temporal ghost imaging; HBTE, Hanbury Brown–Twiss interferometer experiment; BGF, Brillouin gain fiber; RSF, Rayleigh scattering fiber; FWM, four-wave mixing; CSBS, cascaded stimulated Brillouin scattering; OC, optical coupler; SPD, single-photon detector; TCSPC, time-correlated single-photon counter; PD, photodetector.

Route to superbunching

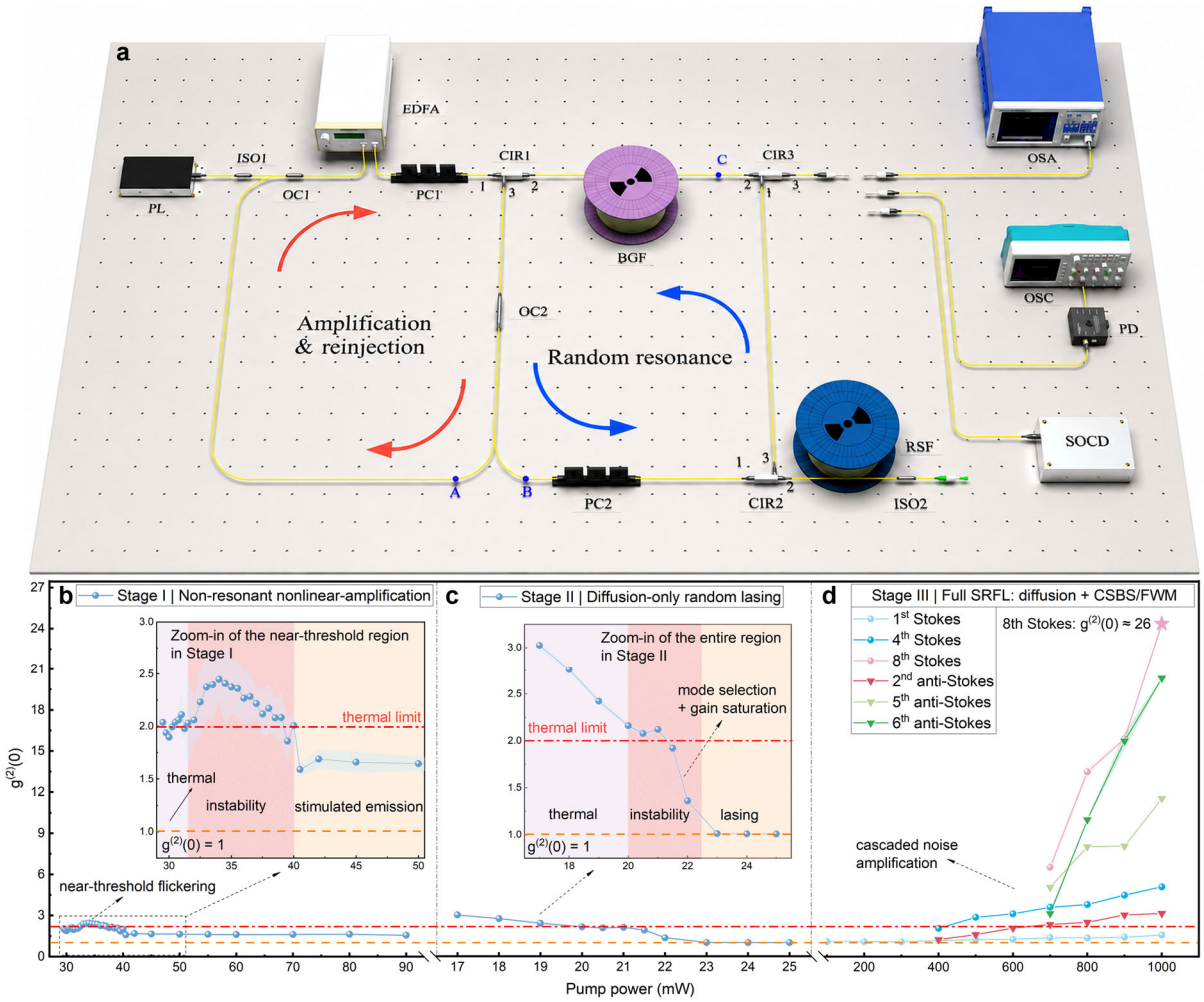


Fig. 2 | Experimental route to superbunching. a, Experimental configuration used to identify the physical ingredients responsible for giant superbunching. Three sequential operational regimes were implemented with progressively increasing feedback and nonlinear complexity. In Stage I, points A, B and C are disconnected, OC2 is removed, and a 5-km single-mode fiber (SMF) serves as the BGF, establishing a non-resonant nonlinear-scattering baseline without random distributed feedback. Stage II, point A is disconnected, points B and C are connected, OC2 is removed, and 5-km and 10-km SMFs serve as the BGF and RSF, respectively. This configuration enables SBS with random distributed feedback. In Stage III, points A, B and C are connected, OC2 is inserted, and a 390-m highly nonlinear fiber and a 10-km SMF serve as the BGF and RSF, respectively. This full SRFL configuration realizes random distributed feedback with co-initiated CSBS and quasi-phase-matched FWM. **b–d,** Three-stage evolution of $g^{(2)}(0)$ as a function of pump power. **b,** Stage I exhibits a transient threshold enhancement followed by relaxation toward the Poissonian limit. **c,** Stage II shows diffusion-enhanced superthermal bunching at low pump power, relaxation toward the thermal Brillouin value, a near-threshold instability and subsequent suppression after resonant random lasing is established. **d,** Stage III exhibits strong pump- and order-dependent growth of $g^{(2)}(0)$, with the 8^{th}-order Stokes component reaching $g^{(2)}(0) \approx 26$. Dashed horizontal lines indicate the Poissonian limit, $g^{(2)}(0) = 1$, and the Gaussian thermal limit, $g^{(2)}(0) = 2$. SOCD, Second-order correlation detection.

To identify the physical ingredients required for giant superbunching, we designed a three-stage experimental route in which random feedback and nonlinear coupling were introduced step by step, while tracking the zero-delay second-order intensity correlation, $g^{(2)}(0)$. The three experimental configurations are summarized in **Fig. 2a**, whereas **Figs. 2b–d** show the associated statistical evolution. Details of the experimental configuration are provided in **Methods**.

Stage I establishes a non-resonant nonlinear-amplification baseline without any additional feedback (**Figs. 2a, b**). In the regime below the SBS threshold, the experimentally retrieved $g^{(2)}(0)$ is close to the thermal value of 2, consistent with thermally seeded spontaneous Brillouin Stokes scattering. Near the SBS threshold, $g^{(2)}(0)$ exceeds the thermal limit and exhibits a transient superthermal spike. This enhancement stems from intermittent burst dynamics, where spontaneously seeded intensity fluctuations undergo transient amplification and induce rapid pump depletion. Upon further pump scaling, the stimulated Brillouin component grows and progressively suppresses the relative contribution of spontaneous thermal fluctuations. At the same time, gain saturation and pump depletion clamp the largest intensity excursions, and thus $g^{(2)}(0)$ decreases from the superthermal peak and settles at a partially bunched value of ~1.6. This value remains above the Poissonian limit because the non-resonant single-pass configuration lacks cavity-mediated mode selection, allowing residual spontaneous-scattering and gain-fluctuation contributions to persist in the emitted Stokes field.

Stage II introduces the RSF to establish Rayleigh-scattering-mediated random lasing in an SBS-dominated configuration, without the additional FWM-assisted nonlinear cascade present in the full SRFL (**Figs. 2a, c**). At the lowest pump powers, $g^{(2)}(0)$ exceeds the thermal limit because the weak, thermally seeded Stokes field undergoes Rayleigh-mediated linear diffusion in the RSF before being fed back to the gain fiber. This diffusion process extends the effective interaction length and redistributes the Stokes field among many indistinguishable scattering trajectories, allowing rare constructive interference events and random-wave interference to generate intermittent intensity bursts. As the pump power increases but remains below the random-lasing threshold, the ordinary spontaneous-Brillouin contribution grows and the detected field samples a larger ensemble of scattering paths and temporal fluctuations, so the excess Rayleigh-feedback-induced intermittency is averaged out and $g^{(2)}(0)$ relaxes toward the thermal Brillouin value of approximately 2. Near the threshold, $g^{(2)}(0)$ rises again owing to the Brillouin-lasing instability and flickering dynamics[29]. As the pump power is further increased, stimulated emission, mode competition and gain saturation suppress the excess intensity fluctuations,

with a corresponding decrease in $g^{(2)}(0)$. This behavior indicates that Rayleigh-mediated linear diffusion enhances noise-seeded intensity fluctuations and promotes superthermal bunching, but in the SBS-dominated random-lasing configuration it does not sustain giant superbunching once the emission becomes resonant.

Stage III represents the complete SRFL architecture, integrating linear diffusion with CSBS and quasi-phase-matched FWM (**Figs. 2a, d**). Rather than undergoing suppression, the stochastic fluctuation seeds generated by linear diffusion are recursively amplified across the cascaded nonlinear processes. Consequently, $g^{(2)}(0)$ increases strongly with pump power and spectral order, with the 8^{th}-order Stokes component reaching $g^{(2)}(0) \approx 26$. This comparative analysis indicates that, whereas the diffusion-only configuration enhances initial bunching but stabilizes the emission once random lasing is established, coupling linear diffusion to cascaded nonlinearities reconfigures the SRFL into a fluctuation-dominated source of superbunched emission.

Spectral-order-resolved photon statistics

Having established the route to superbunching, we next resolve the order-dependent spectral, temporal and statistical signatures of representative Stokes and anti-Stokes lines (**Fig. 3**). **Fig. 3a** shows the full emission spectrum, featuring a dense comb structure composed of eight Stokes and eight anti-Stokes orders. This confirms operation in a regime dominated by strong CSBS and FWM. Prior to temporal and photon-correlation measurements, four representative components—the 6^{th}-order anti-Stokes, 1^{st}-order anti-Stokes, 1^{st}-order Stokes and 8^{th}-order Stokes—are isolated using a tunable optical filter. The filtered spectra in **Figs. 3b1-b4** display narrow, well-resolved and isolated peaks with negligible spectral crosstalk. The corresponding temporal intensity traces in **Figs. 3c1-c4** reveal an order-dependent increase in fluctuation strength. The 1^{st}-order Stokes and anti-Stokes components exhibit moderate, relatively regular fluctuations, whereas the 8^{th}-order Stokes and 6^{th}-order anti-Stokes components show intense, irregular burst-like dynamical behavior. This behavior is consistent with the cascaded nonlinear transfer and amplification of stochastic intensity fluctuations toward higher spectral orders.

The same order-dependent trend is captured by the normalized intensity distributions and second-order coherence functions (**Figs. 3d, e**). As shown in **Fig. 3d3**, the 1^{st}-order Stokes component exhibits an approximately exponential distribution with a relatively short tail, consistent with weakly fluctuating quasi-thermal emission. In contrast, the distributions for the 8^{th}-order Stokes and 6^{th}-order anti-Stokes

components (**Figs. 3d4, d1**) span multiple orders of magnitude in intensity and exhibit prominent heavy-tailed profiles, indicating rare high-intensity bursts generated by cascaded fluctuation amplification. Consistent with these intensity distribution characteristics, the temporal $g^{(2)}(\tau)$ curves in **Figs. 3e1-e4** show that the 1st-order Stokes component exhibits only modest bunching, with $g^{(2)}(0)$ slightly below the thermal value of 2. By contrast, the higher-order components exhibit sharp, prominent peaks at zero delay with $g^{(2)}(0)$ far exceeding 2. These measurements show that extreme photon correlations in the SRFL originate from order-dependent fluctuation transfer across the nonlinear comb, rather than from isolated low-order lasing dynamics.

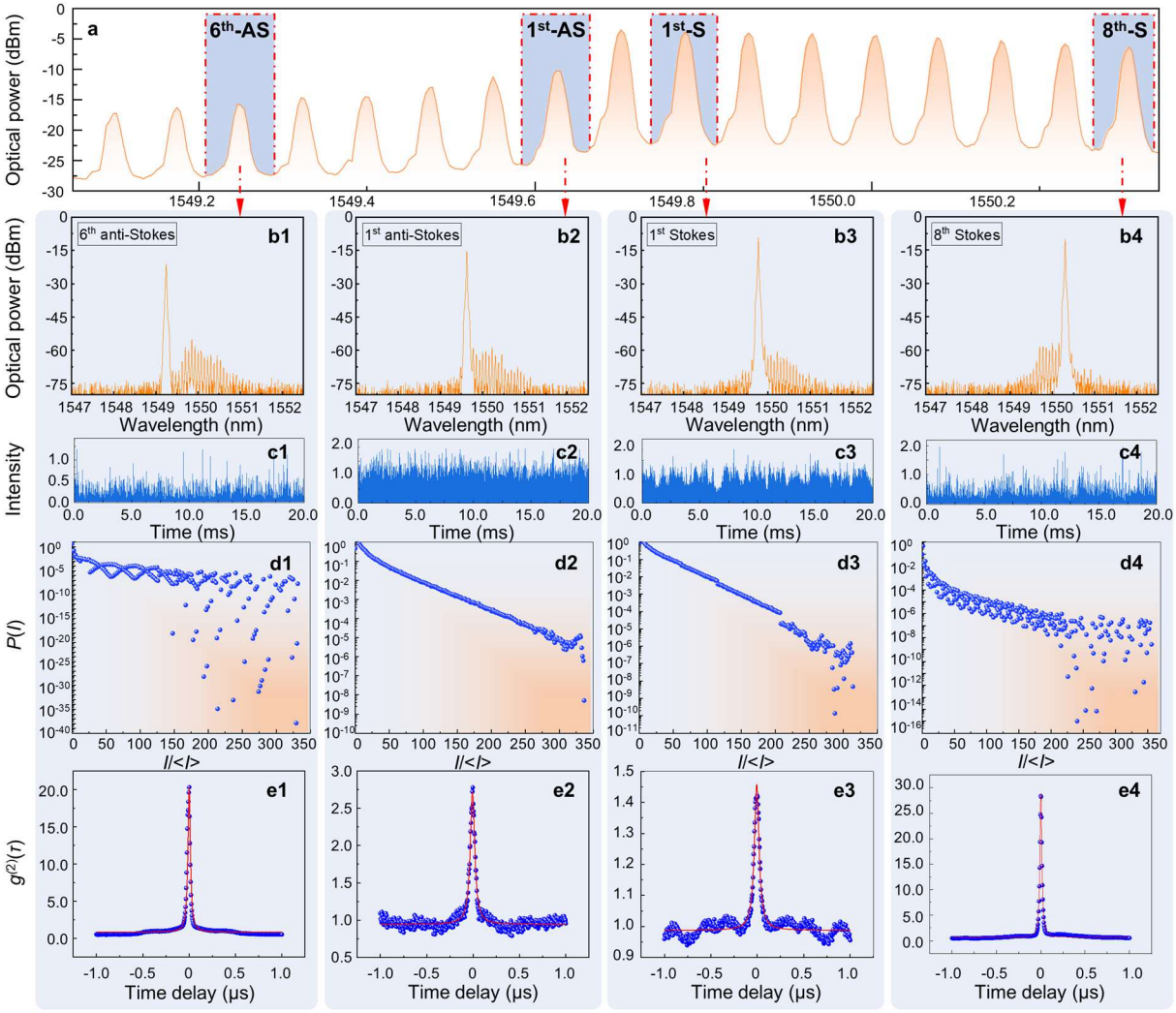


Fig. 3 | Spectral identification and statistical signatures of representative Stokes and anti-Stokes components in the SRFL. a, Full optical emission spectrum of the SRFL. Dashed boxes and arrows highlight four representative spectral components—the 6th-order anti-Stokes, 1st-order anti-Stokes, 1st-order Stokes, and 8th-order Stokes components—selected for detailed characterization. **b1–b4,** Filtered optical spectra corresponding to the four components identified in **a**. **c1–c4,**

Corresponding temporal intensity traces. **d1–d4,** Normalized intensity probability distributions derived from the recorded temporal traces. **e1–e4,** Measured second-order coherence functions, $g^{(2)}(\tau)$, evaluated across the selected cascaded orders.

Parameter-dependent landscape of second-order coherence in the SRFL

To quantitatively characterize the second-order coherence of the SRFL, we mapped the zero-delay second-order coherence $g^{(2)}(0)$ as a two-dimensional parametric landscape governed as a function of pump power, spectral order and RSF length. As illustrated in the parametric maps for a 1-km RSF (**Figs. 4a, b**), all spectral components remain near coherent at low pump powers. However, once the pump power exceeds the threshold for activating deep nonlinear cascades, $g^{(2)}(0)$ rises steeply, especially for higher-order components. A distinct region of giant superbunching emerges in the high-power, high-order domain, indicating that strong pumping and higher-order cascaded nonlinear conversion jointly amplify intensity fluctuations. In support of this conclusion, extending the RSF length to 15 km significantly enhances the achievable superbunching strength (**Figs. 4c, d**), consistent with a denser ensemble of Rayleigh-scattering pathways that supplies stronger stochastic seeds for nonlinear amplification.

To isolate the role of the linear diffusion mechanism, we performed a statistical analysis of coherence for various RSF lengths while maintaining constant spectral conversion efficiency and compared the results with the mirror-based feedback control configuration (0-km RSF). Here, $g^{(2)}(0)_{avg}$ denotes the averaged zero-delay second-order coherence obtained under the same spectral-efficiency condition, allowing a direct comparison of photon statistics among different RSF lengths and spectral orders. As shown in **Figs. 4e and 4f**, the mirror-feedback control yields lower $g^{(2)}(0)_{avg}$ values than the 1-km RSF configuration. Increasing the RSF length further enhances the superbunching magnitude across both the Stokes and anti-Stokes components. The red dashed reference lines in **Figs. 4e and 4f** mark the maximum measured values of 28.67 and 26.27 for the Stokes and anti-Stokes components, respectively. The slight suppression observed for the 7^{th}- and 8^{th}-order anti-Stokes components is attributed to pump-depletion-limited nonlinear transfer, which reduces the driving efficiency of these terminal anti-Stokes components.

These results strongly support the conclusion that both the magnitude and the spectral range of superbunching are governed by the interplay between cascaded nonlinearities and the stochastic fluctuation seeds provided by linear diffusion. This interpretation is consistent with the Heisenberg–

Langevin framework developed in **Methods**, which identifies recursive multiplicative-noise transfer across the nonlinear cascade as the statistical origin of heavy-tailed photon-number distributions. Complementary coupled-wave simulations in **Supplementary Section 1 and Supplementary Fig. 1** reproduce the lower-order Stokes/anti-Stokes dynamical trends and support the experimentally observed order-dependent enhancement of $g^{(2)}(0)$.

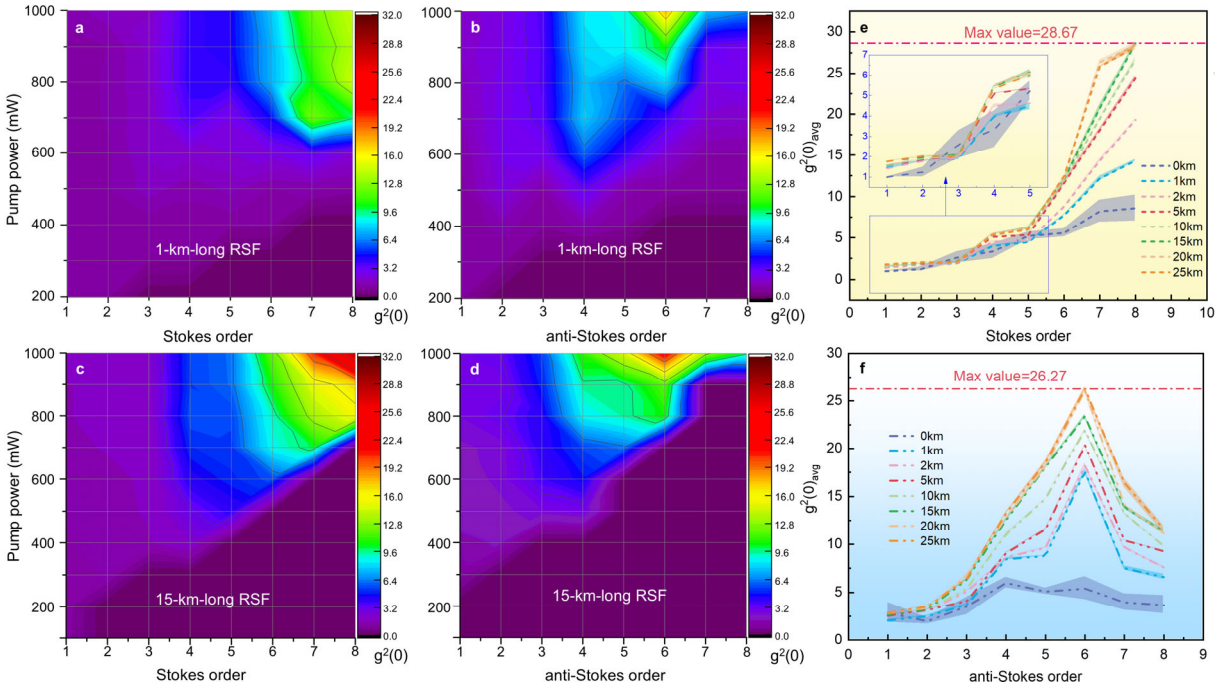


Fig. 4 | Parameter-dependent landscape of second-order coherence in the SRFL. a–d, Two-dimensional color maps of the measured zero-delay second-order coherence, $g^{(2)}(0)$, for Stokes and anti-Stokes components as functions of pump power at RSF lengths of 1-km (**a**, **b**) and 15-km (**c**, **d**). **e,f**, Zero-delay second-order coherence $g^{(2)}(0)$ versus spectral order for various RSF lengths under matched spectral conversion efficiencies. Colored curves represent mean values obtained from ten repeated $g^{(2)}(\tau)$ acquisitions, and the shaded regions with corresponding colors denote the standard deviation. The red dashed lines in **e** and **f** indicate the maximum measured $g^{(2)}(0)$ values of 28.67 and 26.27 for the Stokes and anti-Stokes components, respectively.

Photonic phase evolution and photon statistics

To connect extreme photon statistics with macroscopic cavity dynamics, we correlated the observed superbunching with photonic phase evolution. The computation of the Parisi overlap parameter, the overlap distribution $P(q)$, and the macroscopic overlap $|q|_{avg}$ is described in **Methods. Figs. 5a–d** summarize three characteristic dynamical regimes using four complementary diagnostics: overlap distributions **(Fig. 5a)**, temporal intensity traces **(Fig. 5b)**, replica-correlation heat maps **(Fig. 5c)** and fast Fourier transform spectra **(Fig. 5d)**. The paramagnetic phase is defined by single-mode dominance,

baseline temporal stability, and a Gaussian-like overlap distribution $P(q)$ centered at $q \approx 0$ (**Figs. 5a1-d1**). Conversely, the spin-glass phase emerges via dual resonant mode competition, producing pronounced temporal envelope beating and a bimodal $P(q)$ peaked at ± 1 (**Figs. 5a2-d2**). In the hierarchical non-equilibrium regime, the system exhibits complex multimode oscillations and intermittent bursting, reflected in a fragmented replica-correlation heat map and a broadened $P(q)$ distribution spanning [-1, 1] (**Figs. 5a3-d3**).

We next quantify the interplay between macroscopic phase ordering and microscopic photon correlations. As shown in **Figs. 5e, f,** the macroscopic overlap parameter $|q|_{avg}$ generally decreases as $g^{(2)}(0)$ increases, revealing an overall inverse correlation between replica overlap and photon bunching across the explored operating conditions. This inverse correlation can be understood as a redistribution of accessible fluctuation degrees of freedom in the random cavity. In the spin-glass-like regime, the dynamics are dominated by strongly correlated resonant configurations, leading to large replica overlap. Such correlated phase evolution constrains the accessible intensity configurations and suppresses rare extreme excursions. By contrast, in the hierarchical non-equilibrium regime, replica correlation is weakened and the cavity explores a larger number of short-lived, competing resonant pathways. The resulting frustration and intermittent mode switching increase the probability of rare high-intensity bursts, thereby enhancing the second intensity moment relative to the squared mean intensity and increasing $g^{(2)}(0)$. Thus, giant superbunching is favored in the weakly correlated hierarchical non-equilibrium regime rather than in the strongly correlated spin-glass phase.

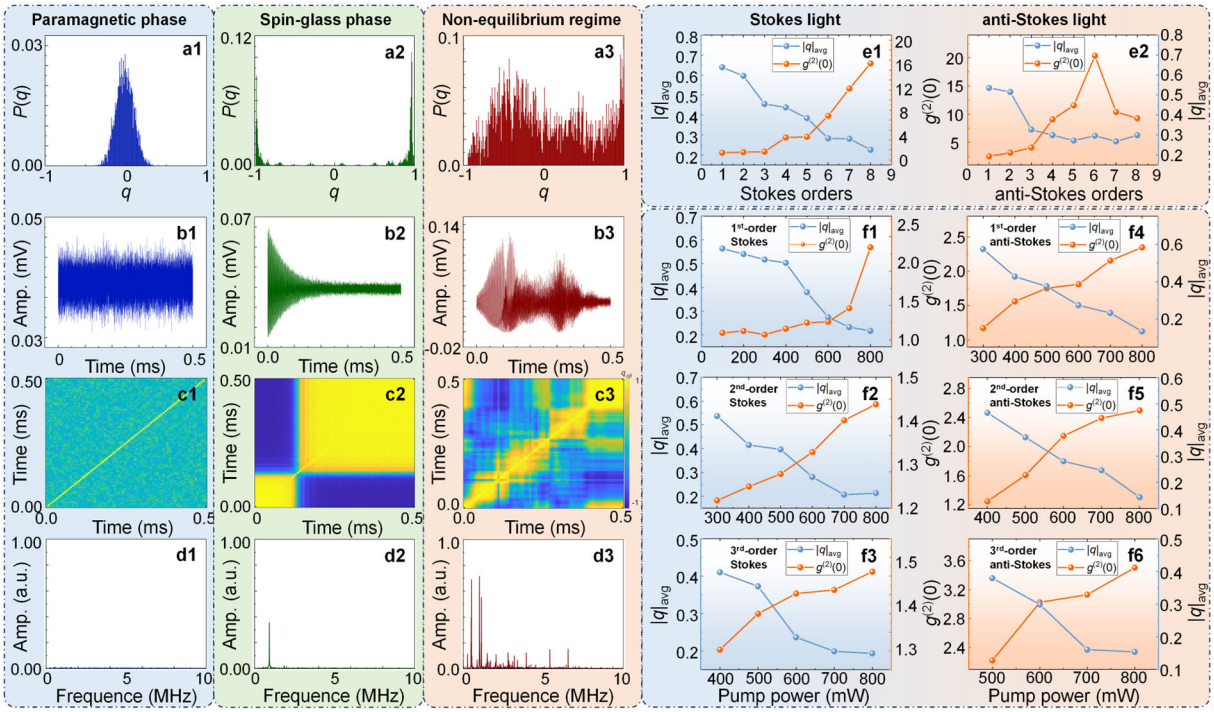


Fig. 5 | Photonic phase signatures and their correlation with extreme photon statistics in the SRFL. a1–a3, Representative overlap distributions, $P(q)$, for three characteristic photonic phase states: the paramagnetic phase (a1), spin-glass phase (a2), and hierarchical non-equilibrium regime (a3). **b1–b3,** Corresponding temporal intensity traces, exhibiting low-amplitude baseline fluctuations, pronounced envelope beating, and burst-like intermittent dynamics, respectively. **c1–c3,** Heat maps of the pairwise Parisi parameter, $q_{\alpha\beta}$, visualizing the distinct replica-correlation structures associated with each phase. **d1–d3,** Corresponding fast Fourier transform spectra, demonstrating single-mode dominance, dual-mode beating, and multimode competition, respectively. **e1, e2,** Evolution of the macroscopic overlap, $|q|_{avg}$ (blue), and the second-order coherence, $g^{(2)}(0)$ (red), as functions of the Stokes (e1) and anti-Stokes (e2) orders. **f1-f6,** Pump-power dependence of $|q|_{avg}$ and $g^{(2)}(0)$ for the 1st-, 2nd-, and 3rd-order Stokes (f1–f3) and anti-Stokes (f4–f6) components. These data reveal an overall inverse correlation between replica overlap and photon bunching, suggesting that giant superbunching is favored when spin-glass-like replica correlations are suppressed and the system evolves toward weakly correlated, hierarchical non-equilibrium dynamics.

Temporal ghost imaging with SRFL

Following the characterization of tunable superbunching, we assess the utility of the SRFL in a correlation-based optical detection architecture. Specifically, selected Stokes and anti-Stokes components with different $g^{(2)}(0)$ values are utilized as structured illumination for TGI. In this configuration, the temporal profile of a target object is reconstructed via intensity correlations rather than direct intensity detection, making the reconstruction quality inherently dependent on the second-order coherence of the illumination source. Representative Stokes and anti-Stokes components were

spectrally filtered and injected into the TGI setup shown in **Fig. 1d**. All TGI measurements were performed using $N = 10{,}000$ independent random temporal intensity patterns, while the average optical power, filter bandwidth and reconstruction parameters were kept identical for all comparisons. These fixed-N measurements were used to compare reconstruction contrast across spectral orders, whereas the reduction in the required number of realizations was evaluated separately by the realization-number-dependent reconstruction analysis in **Supplementary Fig. 4**. Reconstruction quality was quantified by the object-to-background-enhancement signal-to-noise ratio (OBE-SNR), as defined in **Methods**.

The reconstruction performance for different spectral orders is summarized in **Fig. 6**. The retrieved temporal waveforms in **Figs. 6a–f** show a clear improvement in reconstruction contrast from low-order to high-order spectral components. Reconstructions based on low-order components exhibit weak object-to-background contrast, consistent with their relatively small $g^{(2)}(0)$ values. In contrast, high-order Stokes and anti-Stokes components with stronger superbunching yield more pronounced temporal modulation and clearer recovery of the binary target waveform. Importantly, the summary plot in **Fig. 6g** shows that the OBE-SNR increases monotonically with $g^{(2)}(0)$ across the selected spectral components, providing a quantitative correlation between enhanced photon bunching and improved TGI contrast. Separate realization-number-dependent reconstruction measurements in **Supplementary Fig. 4** further show that illumination with larger $g^{(2)}(0)$ reaches comparable high-fidelity reconstruction with more than an order-of-magnitude reduction in the required number of realizations compared with weakly bunched illumination. These results establish a direct quantitative link between engineered photon superbunching and enhanced TGI performance.

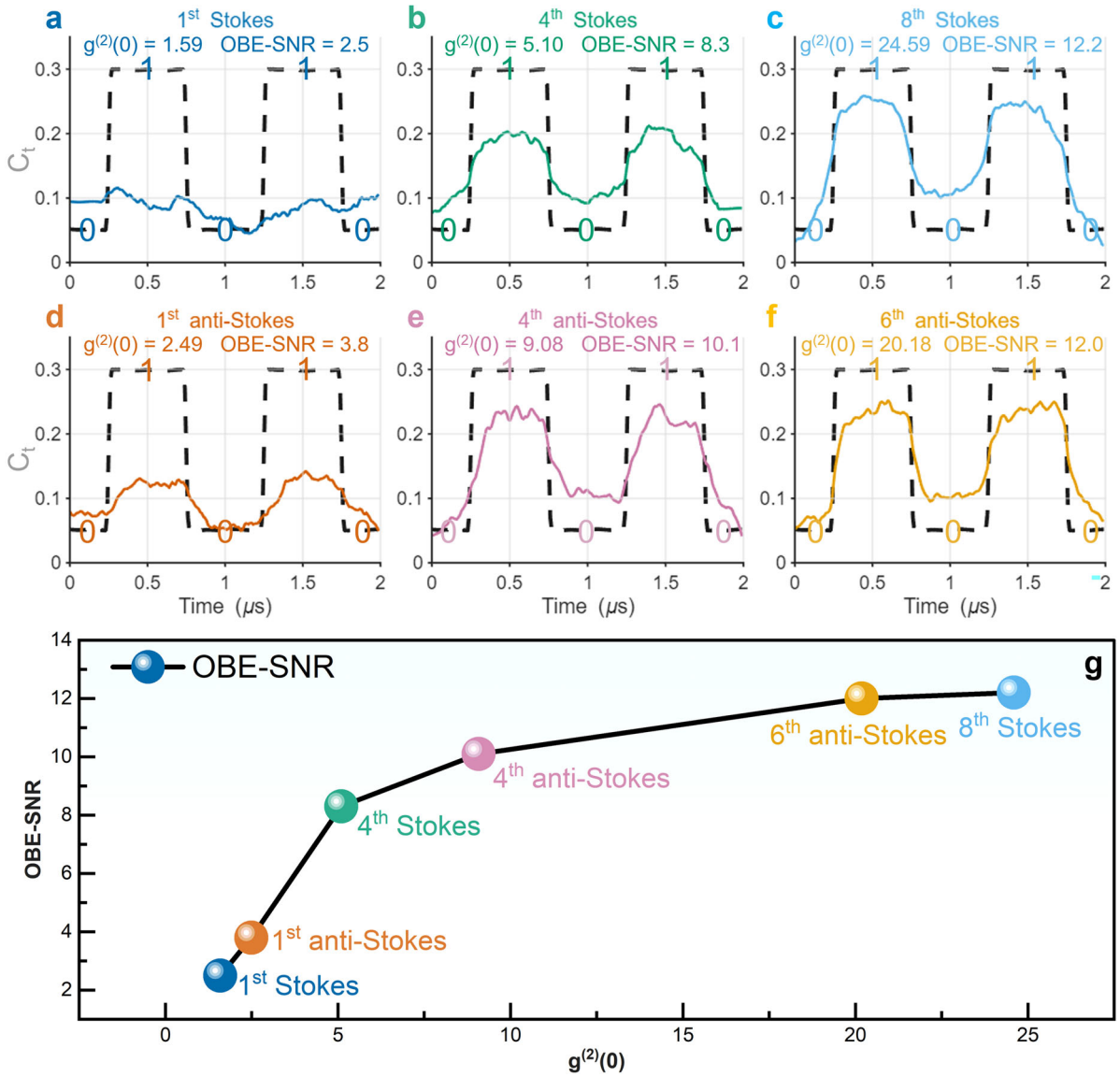


Fig. 6 | Temporal ghost-imaging reconstructions and object-to-background-enhancement signal-to-noise ratio (OBE-SNR) summary using Stokes and anti-Stokes components with different spectral orders. Colored solid curves show the delay-corrected temporal ghost-imaging reconstructions, whereas black dashed curves denote the target binary waveform. All correlation reconstructions were performed with $N = 10{,}000$. The overlaid 0/1 labels denote the temporal binary object encoded in the object arm. **a–c,** Reconstructed temporal waveforms obtained from the 1st-, 4th- and 8th-order Stokes components, respectively. **d–f,** Reconstructed temporal waveforms obtained from the 1st-, 4th- and 6th-order anti-Stokes components, respectively. The measured zero-delay second-order coherence $g^{(2)}(0)$ and the corresponding OBE-SNR are labeled in each panel. The OBE-SNR quantifies the separation between the reconstructed '1' and '0' temporal regions normalized by their residual fluctuations, as defined in **Methods**. **g,** Summary plot of OBE-SNR as a function of $g^{(2)}(0)$ for the six selected spectral components, showing a monotonic increase in reconstruction contrast with increasing photon bunching. Higher-order superbunched components provide higher OBE-SNR and clearer recovery of the target temporal waveform. The realization-

number-dependent reconstruction behavior and the reduction in the required number of realizations are quantified separately in **Supplementary Fig. 4**.

Discussion

This work establishes, to our knowledge, the first all-fiber random-laser platform for reproducibly generating and tuning giant photon superbunching across multiple spectral orders. The key advance is the use of a cooperative linear-nonlinear fluctuation-amplification mechanism: Rayleigh-mediated diffusion provides a controllable stochastic fluctuation reservoir, while CSBS and quasi-phase-matched FWM transfer and amplify these fluctuations across the nonlinear spectral cascade. This mechanism enables photon statistics to be tuned from weakly bunched or nearly coherent emission to giant superbunching with $g^{(2)}(0)$ approaching 28. By combining photon-correlation measurements with Parisi-overlap analysis, we further link the emergence of superbunching to the macroscopic phase evolution of the disordered cavity, connecting random-laser dynamics with measurable high-order photon statistics. Temporal ghost imaging demonstrates the practical value of these engineered statistics, showing that high-order superbunched emission provides higher OBE-SNR and clearer reconstructions than weakly bunched illumination under otherwise identical conditions.

Further improvement will mainly depend on how efficiently the fluctuation cascade can be maintained before pump depletion and finite nonlinear conversion efficiency clamp the terminal Stokes and anti-Stokes orders. Engineering the gain distribution, dispersion and feedback strength should extend both the spectral span and the maximum attainable $g^{(2)}(0)$ and may also enable operation beyond the C-band. A longer-term challenge is to translate the present fiber-based diffusion mechanism to more compact platforms. Integrated Brillouin or Kerr systems offer a possible route but would require on-chip mechanisms that can reproduce strong fluctuation seeding, nonlinear coupling and long-term photon-statistical stability. In parallel, an order-resolved stochastic model that quantitatively links diffusion strength, nonlinear coupling, phase evolution and $g^{(2)}(0)$ will be important for clarifying the scaling limits of superbunching in disordered nonlinear photonic systems.

Methods

System Specifications and Experimental Configuration

The experimental setup of the SRFL, depicted in Fig. 2, uses an all-fiber feedback architecture that

couples a Brillouin gain fiber section to a Rayleigh scattering fiber section through optical couplers and circulators. The RSF provides Rayleigh-scattering-mediated distributed feedback, whereas the additional reinjection path controls the return of the scattered Stokes/anti-Stokes field to the BGF and enables the full SRFL configuration. The system is pumped by a 1550-nm semiconductor laser (LIGHTPROMOTECH, NLLD 0175-3-34-2) featuring a narrow linewidth of ~15 kHz. To safeguard the pump source against detrimental back-reflections, a high-power optical isolator (ISO1) is inserted in the injection path. The pump power is precisely adjusted using an erbium-doped fiber amplifier (EDFA) and a variable optical attenuator. A polarization controller (PC1) is used to optimize the pump polarization, maximizing the efficiency of the polarization-dependent Brillouin scattering process in the gain medium. For the nonlinear gain section, we employ a 390-m highly nonlinear fiber (HNLF) **(**$\geqslant$10 $W^{-1}\cdot km^{-1}$ @1550 nm**)** as the BGF. Random distributed feedback is provided by standard single-mode fiber (SMF-28) of various lengths, acting as the RSF.

The second-order temporal coherence $g^{(2)}(\tau)$ was characterized using a Hanbury Brown–Twiss (HBT) interferometer. To resolve individual spectral components, the SRFL output was spectrally filtered by a tunable optical filter (Alnair Labs, BVF-300CL), which provides continuous bandwidth tuning from 0.03 nm to 3.0 nm. The filter bandwidth was set to approximately 0.1 nm to isolate each selected spectral component with high optical extinction ratio. The filtered light was split and detected by two custom-built InGaAs/InP single-photon detectors (SPDs), and photon arrival times were recorded using a qutools quTAG time-to-digital converter with a digital resolution of 1 ps. Coincidence histograms were accumulated and processed in Daisy software over an integration time of approximately 100 s. The acquisition window contained 256 bins, corresponding to an effective bin width of approximately 3.9 ns, which was sufficient to resolve the $g^{(2)}(\tau)$ peak because the typical coherence time of the SRFL was on the order of tens of nanoseconds. To minimize detector non-idealities and avoid underestimating $g^{(2)}(0)$ during extreme bunching events, the count rate in each detection channel was kept below 150 kHz and a detector dead time of 250 ns was applied to suppress afterpulsing and pulse pile-up. For each operating condition, $g^{(2)}(0)$ was extracted from the zero-delay bin of the corresponding coincidence histogram. Each measurement was repeated independently ten times under identical experimental conditions; the reported $g^{(2)}(0)$ values represent the mean of these repeated acquisitions, and the error bars denote the standard deviation across repeats.

Theoretical framework of the superbunched random fiber laser

To provide a theoretical framework for the photon statistics and the origin of superbunching in the SRFL, we employ a Heisenberg–Langevin formalism for a cascaded open quantum system. The optical field is decomposed into discrete Stokes modes coupled to acoustic phonon modes via CSBS and to a distributed reservoir that provides random Rayleigh feedback. The system dynamics are governed by the total Hamiltonian

$$\hat{H} = \hat{H}_0 + \hat{H}_{CSBS} + \hat{H}_{FWM} + \hat{H}_{RSF}, \tag{1}$$

where the free evolution of the optical modes $\{\hat{a}_n\}$ and acoustic modes $\{\hat{b}_n\}$ is given by

$$\hat{H}_0 = \sum_n \hbar\omega_n \hat{a}_n^\dagger \hat{a}_n + \sum_n \hbar\Omega_n \hat{b}_n^\dagger \hat{b}_n, \tag{2}$$

The interaction between the optical and acoustic fields is mediated by electrostriction, described by the effective CSBS Hamiltonian[29,43]

$$\hat{H}_{CSBS} = \sum_n i\hbar g_{SBS}(\hat{a}_{n-1}\hat{a}_n^\dagger \hat{b}_n^\dagger - \hat{a}_{n-1}^\dagger \hat{a}_n \hat{b}_n), \tag{3}$$

This interaction represents the Stokes process in which a photon at order n-1 is annihilated to create a photon at order n and a phonon. Crucially, the Hermitian conjugate term naturally accounts for the anti-Stokes process, allowing a Stokes photon and a phonon to recombine and regenerate the higher-frequency optical field. The quasi-phase-matched FWM contribution is modeled following the quantum theory of Kerr frequency combs[44]

$$\hat{H}_{FWM} = -\frac{\hbar g_{FWM}}{2} \sum_{n,m,k,l} \delta(m+n-k-l)\hat{a}_n^\dagger \hat{a}_m^\dagger \hat{a}_k \hat{a}_l + h.c., \tag{4}$$

where only mode combinations satisfying the phase-matching condition contribute to the parametric coupling of quantum fluctuations across the cascade.

By eliminating the reservoir degrees of freedom using the input-output formalism[45], we derive the Heisenberg-Langevin equation for the n-th Stokes mode

$$\dot{\hat{a}}_n = -(\frac{\kappa_n}{2} + i\Delta_n)\hat{a}_n + g_{SBS}\hat{a}_{n-1}\hat{b}_n^\dagger - g_{SBS}\hat{a}_{n+1}\hat{b}_{n+1} + \hat{L}_{FWM}(\{a\}) + \hat{F}_{n,RSF}(t) + \hat{F}_{n,vac}(t). \tag{5}$$

Here, κ_n denotes the photon energy decay rate. The noise operators $\hat{F}_{n,RSF}(t)$ and $\hat{F}_{n,vac}(t)$ represent stochastic forces from the Rayleigh scattering reservoir and vacuum fluctuations, respectively. Consistent with the fluctuation-dissipation theorem[45], their correlation functions are

$$\left\langle \hat{F}_{n,RSF}(t)\hat{F}_{m,RSF}(t') \right\rangle = \kappa_n \delta_{nm}\delta(t-t') \tag{6}$$

$$\left\langle \hat{F}_{n,vac}(t)\hat{F}^{\dagger}_{m,vac}(t')\right\rangle = \kappa_n \delta_{nm}\delta(t-t'), \tag{7}$$

The acoustic mode $\hat{b}_n$ is coupled to a thermal phonon bath and obeys the stochastic differential equation in the frame rotating at the acoustic frequency[46,47]

$$\dot{\hat{b}}_n = -(\frac{\Gamma_n}{2} + i\delta_{B,n})\hat{b}_n + g_{SBS}\hat{a}_{n-1}\hat{a}^{\dagger}_n + \hat{G}_n(t), \tag{8}$$

where Γ_n is the acoustic energy damping rate and $\delta_{\mathrm{B,n}}$ represents the acoustic detuning from the Brillouin resonance (assumed to be zero in the resonant approximation). $\hat{G}_n(t)$is the thermal Langevin noise satisfying $\left\langle \hat{G}^{\dagger}_n(t)\hat{G}_m(t')\right\rangle = \Gamma_n n_{th}\delta_{nm}\delta(t-t')$, with n_{th} being the mean thermal phonon occupation.

The statistical properties of the emitted light are characterized by the normalized second-order coherence function defined by Glauber[47]

$$g^{(2)}_n(0) = \frac{\left\langle \hat{a}^{\dagger}_n\hat{a}^{\dagger}_n\hat{a}_n\hat{a}_n\right\rangle}{\left\langle \hat{a}^{\dagger}_n\hat{a}_n\right\rangle^2} \tag{9}$$

In this framework, the effective pump field driving the *n*-th spectral order is not deterministic, but is inherited from the stochastic field of the preceding cascade. The cascaded nonlinear process therefore converts the additive fluctuations introduced by spontaneous Brillouin scattering, Rayleigh backscattering and vacuum noise at lower orders into multiplicative fluctuations at higher orders. Physically, the instantaneous Brillouin gain experienced by a newly generated Stokes order is governed by the fluctuating field amplitude and photon number of the preceding order, whereas quasi-phase-matched FWM redistributes fluctuations among multiple phase-matched Stokes and anti-Stokes components. In both processes, the nonlinear coupling terms contain products of fluctuating field amplitudes, so rare high-intensity events generated at an earlier stage are not simply transferred linearly; they are preferentially amplified in subsequent nonlinear conversion steps and can seed even larger fluctuations in higher orders.

This recursive selection and amplification mechanism causes the higher-order photon-number moments to grow faster than the corresponding powers of the mean photon number, progressively broadening the intensity distribution and producing heavy-tailed statistics. Consequently, the zero-delay second-order coherence, which is governed by the normally ordered second-order photon-number moment, can increase far beyond the Gaussian-statistics thermal limit. This Heisenberg-Langevin formalism thus identifies recursive multiplicative-noise transfer as the statistical origin of photon

superbunching in the SRFL. Rayleigh-mediated linear diffusion supplies the initial stochastic fluctuation reservoir, whereas CSBS and quasi-phase-matched FWM provide the nonlinear pathways that recursively transfer and amplify these fluctuations across the Stokes and anti-Stokes cascade. To complement this fundamental statistical interpretation, a dedicated coupled-wave numerical model incorporating CSBS, quasi-phase-matched FWM, distributed Rayleigh feedback and EDFA gain is developed in **Supplementary Section 1**. The model captures the experimentally observed lower-order dynamical trends and supports the order-dependent increase of $g^{(2)}(0)$, while the Heisenberg-Langevin treatment clarifies why the cascade evolves from ordinary intensity fluctuations into giant superbunched photon statistics.

Computation of the Parisi overlap parameter and $|q|_{avg}$

To quantify photonic phase evolution, we compute the Parisi overlap parameter q using temporal replicas extracted from the detected laser output. A single temporal trace recorded over a wide observation window is divided into N_s replica segments of equal duration. Each replica is treated as an independent realization of the photonic system under identical pumping conditions, consistent with the statistical framework previously applied to Brillouin random fiber lasers[9].

The intensity fluctuation of the α-th replica at sampling index k is defined as

$$\Delta_\alpha(k) = I_\alpha(k) - I(k), \tag{10}$$

where $I_\alpha(k)$ is the replica intensity and $I(k)$ is the ensemble-averaged intensity

$$I(k) = \frac{1}{N_S}\sum_{\alpha=1}^{N_S} I_\alpha(k). \tag{11}$$

The Parisi overlap parameter between two replicas α and β is computed as

$$q_{\alpha\beta} = \frac{\sum_k \Delta_\alpha(k)\Delta_\beta(k)}{\sqrt{(\sum_k \Delta_\alpha^2(k)(\sum_k \Delta_\beta^2(k))}}. \tag{12}$$

For each spectral component, all $N_s(N_s\text{-}1)/2$ overlap values are obtained and their absolute magnitude is averaged to yield a single macroscopic indicator characterizing the correlation strength within the cavity

$$|q|_{avg} = \frac{1}{N_S(N_S-1)/2}\sum_{\alpha<\beta}|q_{\alpha\beta}|. \tag{13}$$

A value of $|q|_{avg}$ approaching zero reflects weak replica correlation, corresponding to a paramagnetic-like photonic state, whereas values close to one indicate strongly correlated replica behavior associated with spin-glass dynamics. Intermediate values correspond to non-equilibrium dynamics characterized

by multimode oscillation and short-lived resonant states.

To visualize the representative photonic phase states (**Figs. 5c1–c3**), we applied the aforementioned Parisi overlap formalism to construct two-dimensional replica-correlation heat maps. Specifically, a broad, continuous temporal intensity trace was truncated to a representative sub-window isolating the target dynamical state, which was then uniformly partitioned into N_s consecutive replica segments of equal duration. The Parisi overlap parameter $q_{\alpha\beta}$ was calculated for every replica pair (α, β) to generate an $N_s \times N_s$ symmetric overlap matrix. The spatial rendering of this matrix resolves the statistical correlation characteristics of the system. Specifically, regions of the heat map near $q = 0$ denote weak replica correlations, whereas values approaching +1 and -1 signify strongly correlated and anti-correlated intensity fluctuations between replica pairs, respectively. Ultimately, this spatial correlation mapping complements the macroscopic scalar $|q|_{avg}$ by revealing the intrinsic replica-correlation topology that underpins the distinct photonic phase states.

Temporal ghost imaging theory

The fundamental principle of TGI is schematically illustrated in the red dashed box in the upper-right panel of **Fig. 1**. The proposed SRFL generates a beam with random intensity fluctuations, which is coupled out and split via a fiber coupler into two separate paths. One beam serves as the reference and is directed to a fast photodiode for real-time recording of temporal intensity fluctuations. The other beam interacts with the temporal signal under test, a bit sequence produced by an ultrafast electro-optic modulator driven by a pulse pattern generator. Following this interaction, the modulated optical signal is collected by a slow photodetector with limited bandwidth that performs temporal integration. Owing to its bandwidth restriction, this detector cannot resolve the fine temporal structure of the optical signal, and instead measures only the total integrated intensity over a full modulation period. This process corresponds to the detection stage of TGI and is mathematically described by

$$S_i = \int_0^{\tau} I_i(t)dt, \tag{14}$$

where $i = 1, 2, \ldots, N$; S_i denotes the integrated intensity measured by the slow detector in the i-th measurement; τ represents the integration time; and $I_i(t)$ corresponds to the signal after the interaction between the light source and the temporal signal under test, which is expressed as

$$I_i(t) = P_i(t)C(t). \tag{15}$$

Here, $P_i(t)$ represents the waveform of the optical signal with random intensity fluctuations recorded by

the fast detector, $C(t)$ denotes the temporal signal under test, and the product $P_i(t)C_t$ represents pointwise multiplication between the two sequences. After N repeated measurements, the target temporal signal $C'(t)$ can be reconstructed through correlation analysis between the simultaneously acquired sequences from both branches. This reconstruction is expressed as

$$C'(t) = \left\langle (S_i - \left\langle S_i \right\rangle)(P_i(t) - \left\langle P_i(t) \right\rangle) \right\rangle, \tag{16}$$

where the angle brackets ⟨⟩ denote the ensemble average over N measurements, equivalent to the expectation value.

For the reconstructions shown in **Fig. 6**, N = 10,000 independent realizations were used for each selected Stokes or anti-Stokes component. To ensure that the comparison primarily reflected the intrinsic photon statistics of the illumination source rather than differences in optical power or detection conditions, the filtered optical power incident on the TGI setup was adjusted to the same level for all selected components. The same filter bandwidth, temporal object, acquisition window, delay-correction procedure and reconstruction algorithm were used throughout. Additional realization-number-dependent reconstruction measurements were performed by varying the number of realizations while keeping the same reconstruction pipeline, allowing the averaging requirement of weakly bunched and strongly superbunched illumination to be compared under otherwise identical conditions.

To quantify the reconstruction quality of the binary temporal object, we calculated the OBE-SNR from the delay-corrected TGI correlation trace. The target temporal object consists of two types of time windows: object windows, corresponding to the '1' regions, and background windows, corresponding to the '0' regions. These two sets of sampling points are denoted as Ω_1 and Ω_0, respectively. For the reconstructed correlation trace C_t, we calculated the mean amplitudes in the object and background regions as

$$\bar{C}_1 = \frac{1}{N_1}\sum\nolimits_{t_i \in \Omega_1} C_{t_i}, \quad \bar{C}_0 = \frac{1}{N_0}\sum\nolimits_{t_i \in \Omega_0} C_{t_i}, \tag{17}$$

where N_1 and N_0 are the numbers of sampling points in Ω_1 and Ω_0, respectively. The corresponding standard deviations are

$$\sigma_1 = \sqrt{\frac{1}{N_1 - 1}\sum\nolimits_{t_i \in \Omega_1} (C_{t_i} - \bar{C}_1)^2}, \quad \sigma_0 = \sqrt{\frac{1}{N_0 - 1}\sum\nolimits_{t_i \in \Omega_0} (C_{t_i} - \bar{C}_0)^2}. \tag{18}$$

The OBE-SNR was then defined as

$$\mathrm{OBE-SNR} = \frac{\bar{c}_1 - \bar{c}_0}{\sqrt{\sigma_1^2 + \sigma_0^2}}. \tag{19}$$

This definition quantifies how many effective noise levels separate the reconstructed object and background amplitudes. A larger OBE-SNR therefore indicates stronger separation between the reconstructed '1' and '0' temporal regions and corresponds to a higher-contrast reconstruction of the binary temporal waveform. For the realization-number-dependent reconstruction in **Supplementary Fig. 4**, the same delay-correction and OBE-SNR evaluation procedure was applied to reconstructions obtained with different numbers of realizations. This analysis was used to compare the number of realizations required to reach comparable reconstruction fidelity for weakly bunched and strongly superbunched illumination.

Competing interests

The authors declare no competing interests.

Data availability

The data supporting the findings of this study, including the photon-correlation histograms, temporal traces, reconstructed temporal ghost-imaging data and processed datasets used to generate the figures, are available from the corresponding author upon reasonable request. Source data for the main figures are provided with this paper.

References

1. Turitsyn, S. K. et al. Random distributed feedback fibre laser. *Nat. Photon.* **4**, 231–235 (2010).
2. Churkin, D. V. et al. Recent advances in fundamentals and applications of random fiber lasers. *Adv. Opt. Photon.* **7**, 516–569 (2015).
3. Gomes, A. S. L., Moura, A. L., De Araújo, C. B. & Raposo, E. P. Recent advances and applications of random lasers and random fiber lasers. *Prog. Quantum Electron.* **78**, 100343 (2021).
4. Abaie, B. et al. Random lasing in an Anderson localizing optical fiber. *Light Sci. Appl.* **6**, e1704 (2017).
5. Pang, Y. et al. Unveiling optical rogue wave behavior with temporally localized structures in Brillouin random fiber laser comb. *Adv. Photon. Nexus* **3**, 026008 (2024).
6. Xu, J. et al. Optical rogue wave in random fiber laser. *Photon. Res.* **8**, 1-7 (2020).
7. Qi, Y. et al. Replica symmetry breaking in 1D Rayleigh scattering system: theory and validations.

Light Sci. Appl. **13**, 151 (2024).

8. Zhang, L. et al. Transient replica symmetry breaking in Brillouin random fiber lasers. *PhotoniX* **4**, 33 (2023).
9. Ji, Q. et al. Observed photonic phase evolutions in Brillouin random fiber laser comb. *Chin. J. Phys.* **98**, 287–298 (2025).
10. Wiersig, J. et al. Direct observation of correlations between individual photon emission events of a microcavity laser. *Nature* **460**, 245–249 (2009).
11. Reinhard, A. et al. Strongly correlated photons on a chip. *Nat. Photon.* **6**, 93–96 (2012).
12. Pang, Y. et al. Parallel fast random bit generation based on spectrotemporally uncorrelated random laser comb. *Laser Photonics Rev.* **19,** e00675 (2025).
13. Pang, Y. et al. Frequency comb generation based on Brillouin random lasing oscillation and four-wave mixing assisted with nonlinear optical loop mirror. *Photonics* **10**, 296 (2023).
14. Zhang, L. et al. Multi-wavelength Brillouin random fiber laser via distributed feedback from a random fiber grating. *J. Lightwave Technol.* **36**, 2122–2128 (2018).
15. Pang, M. et al. Frequency stabilized coherent Brillouin random fiber laser: theory and experiments. *Opt. Express* **21**, 27155–27168 (2013).
16. Pang, M., Bao, X. & Chen, L. Observation of narrow linewidth spikes in the coherent Brillouin random fiber laser. *Opt. Lett.* **38**, 1866–1868 (2013).
17. Biasco, S. et al. Frequency-tunable continuous-wave random lasers at terahertz frequencies. *Light Sci. Appl.* **8**, 43 (2019).
18. Vojta, T. Disorder in quantum many-body systems. Annu. Rev. Condens. *Matter Phys.* **10**, 233–252 (2019).
19. Hanzo, L. et al. Quantum information processing, sensing, and communications: their myths, realities, and futures. *Proc. IEEE* **113**, 1024–1074 (2025).
20. Smith, J. et al. Many-body localization in a quantum simulator with programmable random disorder. *Nat. Phys.* **12**, 907–911 (2016).
21. Hanbury Brown, R. & Twiss, R. Q. A test of a new type of stellar interferometer on Sirius. *Nature* **178,** 1046–1048 (1956).
22. Hanbury Brown, R. & Twiss, R. Q. Correlations between photons in two coherent beams of light. *Nature* **177**, 27–29 (1956).

552 23. Glauber, R. J. Photon correlations. *Phys. Rev. Lett.* **10**, 84–86 (1963).
553 24. Bromberg, Y., Lahini, Y., Small, E. & Silberberg, Y. Hanbury Brown and Twiss interferometry with
554 interacting photons. *Nat. Photon.* **4**, 721–726 (2010).
555 25. Mikhalychev, A. B. et al. Efficiently reconstructing compound objects by quantum imaging with
556 higher-order correlation functions. *Commun. Phys.* **2**, 134 (2019).
557 26. Shih, Y. Quantum Imaging. Preprint at arXiv:0707.0268 (2007).
558 27. Lubin, G., Oron, D., Rossman, U., Tenne, R. & Yallapragada, V. J. Photon correlations in
559 spectroscopy and microscopy. *ACS Photonics* **9**, 2891–2904 (2022).
560 28. Kimble, H. J., Dagenais, M. & Mandel, L. Photon antibunching in resonance fluorescence. *Phys.*
561 *Rev. Lett.* **39**, 691–695 (1977).
562 29. Cryer-Jenkins, E. A. et al. Second-order coherence across the Brillouin lasing threshold. *Optica* **10**,
563 1432–1438 (2023).
564 30. Hayenga, W. E. et al. Second-order coherence properties of metallic nanolasers. *Optica* **3**, 1187–
565 1193 (2016).
566 31. Zhang, S. et al. Controllable superbunching effect from four-wave mixing process in atomic vapor.
567 *Opt. Express* **28**, 21489–21498 (2020).
568 32. Couto, O. D. D. et al. Photon anti-bunching in acoustically pumped quantum dots. *Nat. Photon.* **3**,
569 645–648 (2009).
570 33. Wang, Z. et al. Optically driven giant superbunching from a single perovskite quantum dot. *Adv. Opt.*
571 *Mater.* **9**, 2100879 (2021).
572 34. Bai, B. et al. Two-photon superbunching of pseudothermal light in a Hanbury Brown-Twiss
573 interferometer. *J. Opt. Soc. Am. B* **34**, 2081–2088 (2017).
574 35. Zhang, L. et al. Superbunching effect of classical light with a digitally designed spatially phase-
575 correlated wave front. *Phys. Rev. A* **99**, 063827 (2019).
576 36. Zhou, Y. et al. Superbunching pseudothermal light. *Phys. Rev. A* **95**, 053809 (2017).
577 37. Hong, P., Liu, J. & Zhang, G. Two-photon super bunching of thermal light via multiple two-photon-
578 path interference. *Phys. Rev. A* **86**, 013807 (2012).
579 38. Zhou, Y. et al. Superbunching pseudothermal light with intensity modulated laser light and rotating
580 groundglass. *Opt. Commun.* **437**, 330–336 (2019).
581 39. Zhou, Y. et al. Experimental observation of three-photon superbunching in linear optical system. *J.*

582 *Opt. Soc. Am. B* **36**, 96–100 (2019).
583 40. Shapiro, J. H. Computational ghost imaging. *Phys. Rev. A* **78**, 061802 (2008).
584 41. Ryczkowski, P., Barbier, M., Friberg, A. T., Dudley, J. M. & Genty, G. Ghost imaging in the time
585 domain. *Nat. Photon.* **10**, 167–170 (2016).
586 42. Ferri, F., Magatti, D., Lugiato, L. A. & Gatti, A. Differential ghost imaging. *Phys. Rev. Lett.* **104**,
587 253603 (2010).
588 43. Behunin, R. O., Otterstrom, N. T., Rakich, P. T., Gundavarapu, S. & Blumenthal, D. J. Fundamental
589 noise dynamics in cascaded-order Brillouin lasers. *Phys. Rev. A* **98**, 023832 (2018).
590 44. Chembo, Y. K. Quantum dynamics of Kerr optical frequency combs below and above threshold:
591 Spontaneous four-wave mixing, entanglement, and squeezed states of light. *Phys. Rev. A* **93**, 033820
592 (2016).
593 45. Collett, M. J. & Gardiner, C. W. Squeezing of light by parametric amplification in an optical cavity.
594 *Phys. Rev. A* **30**, 1386–1391 (1984).
595 46. Gaeta, A. L. & Boyd, R. W. Stochastic dynamics of stimulated Brillouin scattering in an optical fiber.
596 *Phys. Rev. A* **44**, 3205–3209 (1991).
597 47. Glauber, R. J. The quantum theory of optical coherence. *Phys. Rev.* **130**, 2529–2539 (1963).

Supplementary Files

This is a list of supplementary files associated with this preprint. Click to download.

- SupplementarySuperbunchedRandomFiberLaser.docx
- NPHOT20260501398SI.pdf